

Comparative study of the experimentally observed and GAN-generated 3D microstructures in dual-phase steels

Ikumu Watanabe ^a, Keiya Sugiura^b, Ta-Te Chen ^b, Toshio Ogawa ^b and Yoshitaka Adachi ^b

^aCenter for Basic Research on Materials, National Institute for Materials Science, Tsukuba, Japan;

^bGraduate School of Engineering, Nagoya University, Nagoya, Japan

ABSTRACT

In a deep-learning-based algorithm, generative adversarial networks can generate images similar to an input. Using this algorithm, an artificial three-dimensional (3D) microstructure can be reproduced from two-dimensional images. Although the generated 3D microstructure has a similar appearance, its reproducibility should be examined for practical applications. This study used an automated serial sectioning technique to compare the 3D microstructures of two dual-phase steels generated from three orthogonal surface images with their corresponding observed 3D microstructures. The mechanical behaviors were examined using the finite element analysis method for the representative volume element, in which finite element models of microstructures were directly constructed from the 3D voxel data using a voxel coarsening approach. The macroscopic material responses of the generated microstructures captured the anisotropy caused by the microscopic morphology. However, these responses did not quantitatively align with those of the observed microstructures owing to inaccuracies in reproducing the volume fraction of the ferrite/martensite phase. Additionally, the generation algorithm struggled to replicate the microscopic morphology, particularly in cases with a low volume fraction of the martensite phase where the martensite connectivity was not discernible from the input images. The results demonstrate the limitations of the generation algorithm and the necessity for 3D observations.

ARTICLE HISTORY

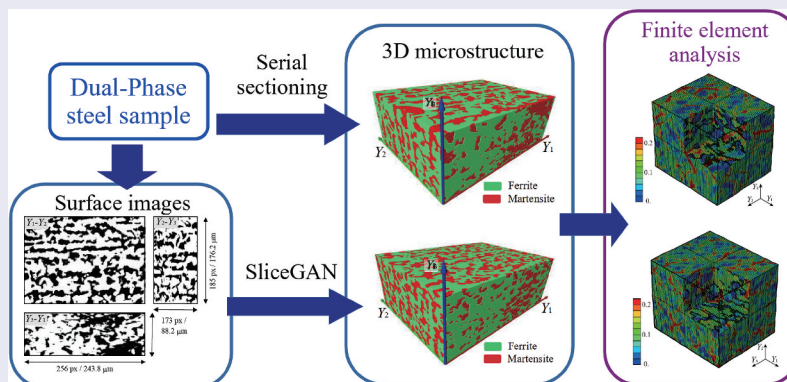
Received 17 April 2024

Revised 4 July 2024

Accepted 31 July 2024

KEYWORDS

3D microstructure generation; image-based finite element analysis; multiscale modeling; anisotropy; dual-phase steels





IMPACT STATEMENT

This study provided the comparison between experimentally observed and computationally generated 3D microstructures of dual-phase steels in the macro- and microscopic material behaviors with finite element analysis method for periodic microstructure.

1. Introduction

The macroscopic properties of materials are strongly influenced by their microscopic heterogeneity. In the so-called metamaterials, unique material properties, such as a negative Poisson's ratio [1,2] and a highly variable stiffness [3], can be realized by controlling microscopic heterogeneity rather than the intrinsic physical properties. Topology optimization, a well-established computer-oriented design method rooted in the finite element method and mathematical

optimization theory, has founded applications in materials research and development (R&D), including industrial design [4]. Recently, there have been advancements in deep-learning-based design approaches [5,6], enabling the design of microstructures based on these computational methods. However, a considerable challenge that persists is the fabrication of these designed microstructures. Despite the additive manufacturing technology enabling the fabrication of structures with complicated

CONTACT Ikumu Watanabe  WATANABE.Ikumu@nims.go.jp  Center for Basic Research on Materials, National Institute for Materials Science, 1-2-1 Sengen, Tsukuba 305-0047, Japan

© 2024 The Author(s). Published by National Institute for Materials Science in partnership with Taylor & Francis Group.

This is an Open Access article distributed under the terms of the Creative Commons Attribution-NonCommercial License (<http://creativecommons.org/licenses/by-nc/4.0/>), which permits unrestricted non-commercial use, distribution, and reproduction in any medium, provided the original work is properly cited. The terms on which this article has been published allow the posting of the Accepted Manuscript in a repository by the author(s) or with their consent.

microstructures, there remain practical limitations, such as the available materials and sample size.

Metallic materials, such as steels, are among the most important structural materials in the industry. In the R&D of metallic materials, controlling microscopic heterogeneity is a major technique for improving the mechanical properties, as represented by the process – structure – properties – performance reciprocity [7,8]. In this context, various processes have been developed to fabricate a controlled microstructure [9,10]. Watanabe et al. (2015) [11] designed a duplex microstructure that maximized macroscopic strength using topology optimization. Similar to the optimized microstructure, Orlov and Ameyama (2020) [12] developed materials with a harmonic microstructure and enhanced their mechanical properties, including strength, fatigue, and corrosion resistance. The process-oriented microstructure control has the potential to improve mechanical properties without adding alloy elements.

Characterization of the three-dimensional (3D) microstructure is required to ensure microscopic morphology, which is an important technology in the R&D of microstructure control. A micrograph of the sample surface is used to characterize the microstructure; however, the surface does not represent the overall 3D microstructure. For instance, microstructures with anisotropic features cannot reproduce a single surface micrograph. Therefore, various technologies have been developed to characterize 3D microstructures. X-ray computed tomography can provide non-destructive 3D data, enabling in-situ material tests [13,14]. Additionally, destructive approaches based on serial sectioning technologies have been established. Sato et al. (2012) [15] characterized 3D microstructures using an automated system based on surface polishing and optical microscopy. Nishikawa et al. (2023) [16] observed a 3D fatigue crack in a superalloy using an Xe plasma-focused ion beam scanning electron microscope system. Despite its feasibility, the characterization of 3D microstructures demands massive effort using special equipment.

Computational approaches have been developed to streamline the reconstruction of 3D microstructures. Turner and Kalidindi [17], as well as Fu et al. [18], have demonstrated efficient reconstruction algorithms that derive 3D microstructures from statistical geometric parameters obtained from a small number of 2D cross-sectional images. Bostanabad [19] proposed a machine-learning-based algorithm using 2D microstructure images for training 3D reconstruction models. The field of 3D reconstruction from 2D images has garnered substantial attention, particularly with the application of deep-learning-based approaches poised to revolutionize this domain. Generative adversarial networks (GANs) are effective unsupervised learning algorithms, leveraging adversarial training to handle

diverse data types such as texts, images, and music. Recently, these technologies have been applied to 3D reconstruction from 2D images. For instance, Zhang et al. [20] developed an algorithm combining variational autoencoder and GAN to reconstruct 3D porous microstructures from 2D slice images. In another innovative approach, Kench and Cooper (2021) [21] introduced SliceGAN, a novel GAN-based algorithm designed to generate 3D microstructures from cross-sectional micrographs. SliceGAN features a 3D generator and a 2D discriminator, resolving the dimensional disparity between 2D training images and 3D generated volumes through a slicing mechanism. SliceGAN has been successfully employed to generate a diverse array of materials, ranging from polycrystalline aggregates to perovskite ceramics, carbon fiber rods, battery separators, and battery cathodes [21]. Furthermore, Sugiura et al. (2022) [22] extended SliceGAN to an algorithm for generating 3D microstructures with anisotropic features from three cross-sectional micrographs of orthogonal surfaces. This algorithm was also applied to generate microstructures of the additive-manufactured samples [23]. As mentioned, these algorithms can generate 3D microstructures from 2D images. However, the validity and reliability of these algorithms still need to be thoroughly investigated and validated.

This study validated the generated 3D microstructures of two types of ferrite – martensite dual-phase steels by comparing them with the experimentally observed 3D microstructure. The macroscopic properties were examined using the image-based finite element analyses. The applicability of the generation algorithm is discussed based on the comparison results. The flowchart of this study is illustrated in Figure 1.

2. Finite element modeling of dual-phase microstructures

Finite element models of dual-phase microstructures were constructed from the 3D voxel data that were experimentally obtained using an automated serial sectioning system and computationally generated from cross-sectional micrographs using SliceGAN.

2.1. Samples of dual-phase steels

Two types of ferrite – martensite dual-phase steels, DP1 and DP2, were prepared as the samples. Their chemical compositions are detailed in Table 1. Subsequently, these samples underwent annealing at 1473 K for 1 h, followed by hot-rolling in the austenite region and air-cooling to 923 K, then water-cooling to 298 ± 2 K. The prior austenite and ferrite grain sizes in both samples were approximately 50 μm and 22 μm , respectively. DP1 was characterized by an isotropic microstructure containing a low volume fraction of

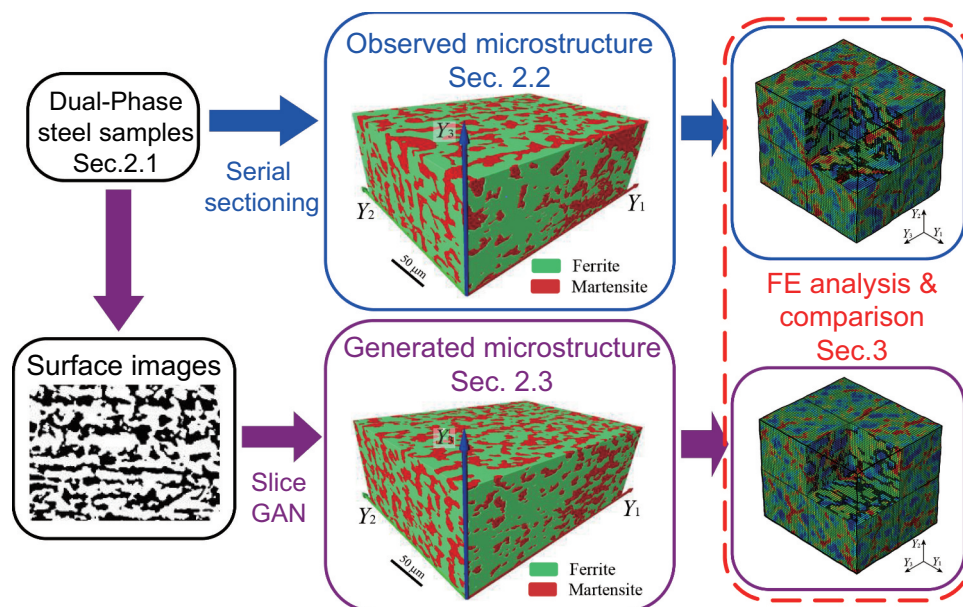


Figure 1. Flowchart of this study.

Table 1. Chemical compositions of dual-phase steel samples.

[wt%]	C	Si	Mn	P	S	Al	N
DP1	0.05	0.49	2.01	<0.001	0.0010	0.031	0.0016
DP2	0.10	0.50	1.99	<0.001	0.0010	0.030	0.0021

the martensite phase. DP2 had an anisotropic microstructure with a larger volume fraction of the martensite phase.

In dual-phase steels, the effect of the microscopic heterogeneities on the macroscopic mechanical properties has been investigated. Finite element analysis based on experimental observation addressed the morphological effect, and numerous studies have explored 2D microstructures [24–28]. Matsuno et al. [29] generated artificial 3D microstructures of dual-phase steels using the Voronoi diagram and conducted deformation analyses; however, such a mathematical patterning could not reproduce the actual morphology. In this study, 3D microstructures of DP1 and DP2 were generated from cross-sectional micrographs using a deep-learning-based generation algorithm. Additionally, the actual 3D microstructures were experimentally observed for comparison.

The 3D microstructures were obtained using an automated serial sectioning system based on an optical microscope and machine-learning-based phase recognition [15,22]. Figure 2 shows the observed 3D microstructures, indicating the phase-maps of the surface of the rectangular space (a) and 3D distributions of the martensite phase in space (b). In Figure 2(b), the connected aggregates of the martensite phase are classified by color. The martensite phases in DP1 and DP2 are connectively distributed; the former is randomly distributed, whereas the latter exhibits a plate-like structure.

2.2. Generation of 3D microstructures

The 3D microstructures of DP1 and DP2 were generated using SliceGAN based on three orthogonal images [22], in which the phase-maps on the surface of the rectangular space, as shown in Figure 2 (a1) and (a2), were used as input. The images had the scales $243.8 \mu\text{m} \times 176.2 \mu\text{m} \times 67.1 \mu\text{m}$ and $243.8 \mu\text{m} \times 176.2 \mu\text{m} \times 88.2 \mu\text{m}$ in DP1 and DP2, respectively. However, they were adjusted to the same resolution of $256 \text{ pixels} \times 185 \text{ pixels} \times 172$ or 173 pixels to capture the microscopic morphology with limited computational efforts, as shown in Figure 3. Table 2 summarizes the volume fractions of martensite phase in the input images, which varied between 13.98% and 15.76% in DP1 and 35.75% and 40.54% in DP2. The difference in volume fraction observed in the input images roughly indicates the magnitude of anisotropy. Specifically, these differences are 1.78% in DP1 and 4.79% in DP2, respectively, consistent with the earlier descriptions regarding the geometric characteristics of microstructures in DP1 and DP2. Figure 4 shows the generated microstructures. In Figure 4(b), the connected aggregates of the martensite phase are classified by color. The algorithm exhibits diversity in its generated results, as illustrated in Figure 4, which showcases representative outcomes.

Table 3 summarizes the volume fraction and number of grains of martensite phase in the observed and generated microstructures. The volume fractions of martensite phase in generated microstructures were

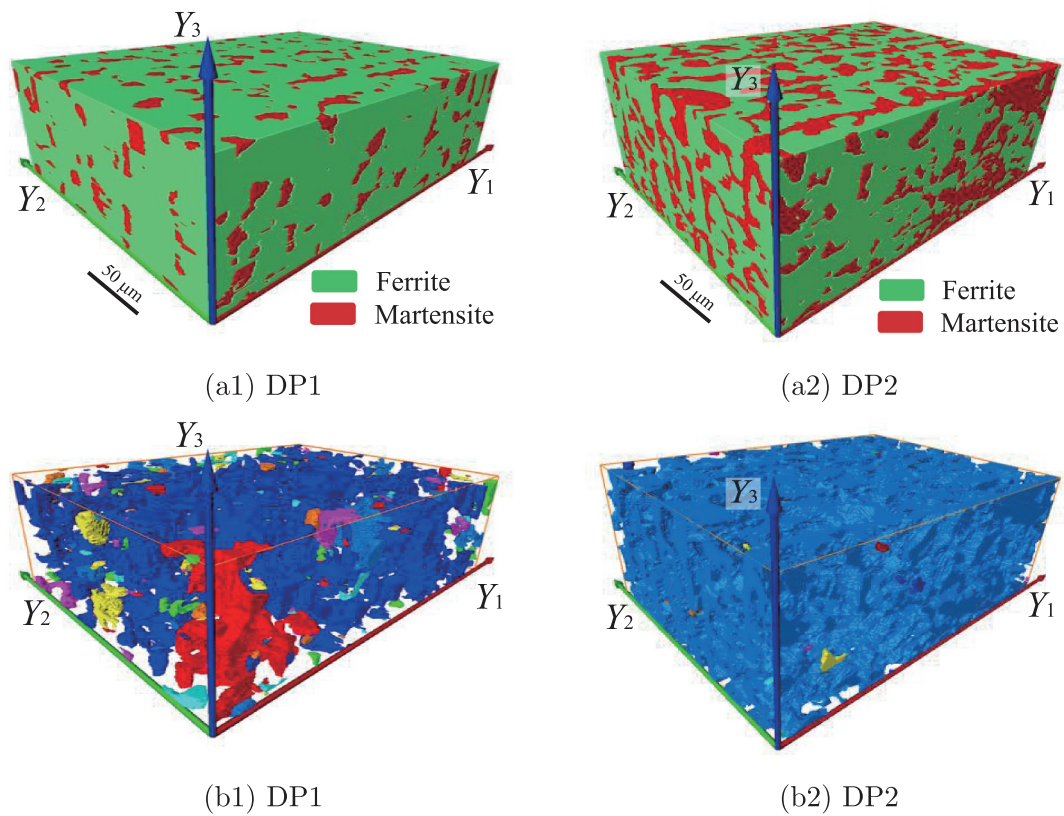


Figure 2. 3D microstructure observation of dual-phase steels: (a) phase maps of the three orthogonal surfaces and (b) 3D distributions of the martensite phase in which the connected aggregates are classified based on color.

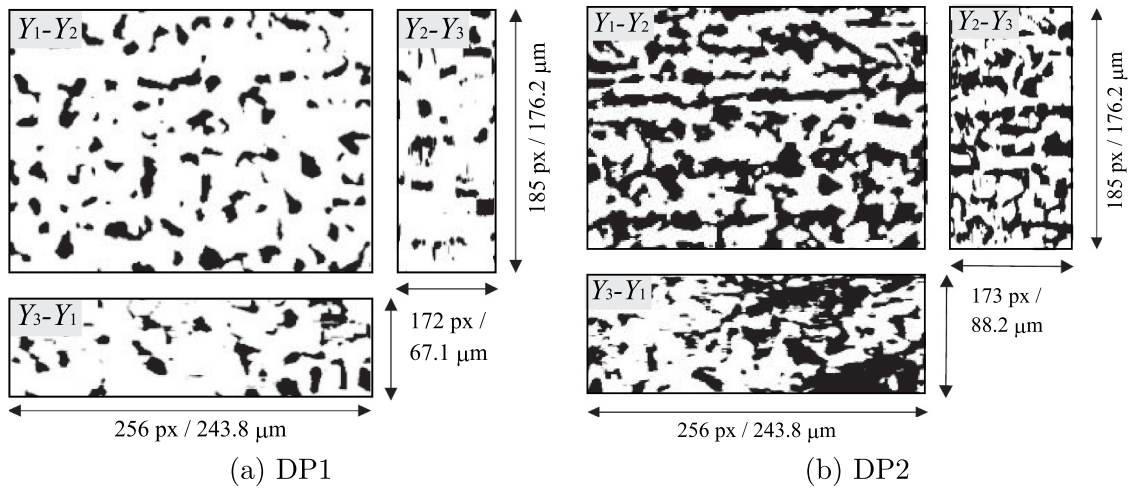


Figure 3. Input images for microstructure generation.

Table 2. Volume fraction of the martensite phase in input images.

Volume fraction [%]	DP1			DP2		
	Y_1-Y_2	Y_2-Y_3	Y_3-Y_1	Y_1-Y_2	Y_2-Y_3	Y_3-Y_1
	15.31	13.98	15.76	40.54	35.75	38.46

of those of input images in both DP1 and DP2. Eventually, the volume fractions were different from the observed 3D microstructures. This limitation arises because SliceGAN generates 3D microstructure

without considering the volume fraction. Technically, performance could be enhanced by developing an algorithm that incorporates constraints related to volume fraction.

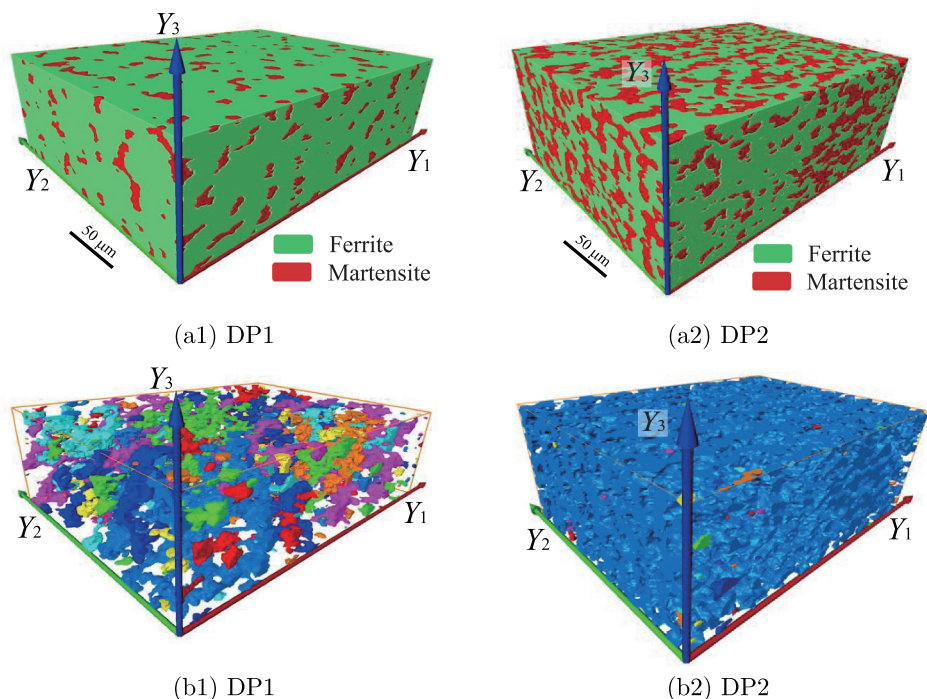


Figure 4. 3D microstructure generation of dual-phase steels: (a) phase maps of the three orthogonal surfaces and (b) 3D distributions of the martensite phase in which the connected aggregates are classified based on color.

Table 3. Volume fraction and number of grains of the martensite phase in the observed and generated 3D microstructures.

	DP1		DP2	
	Observed	Generated	Observed	Generated
Volume fraction [%]	13.9	10.4	39.5	42.1
Number of grains	635	609	84	147

In DP1, the morphology of the martensite phase differed between the observed and generated 3D microstructures. Figures 2(b) and 4(b) illustrate that in the observed microstructure, the martensite phase was distributed in a connected manner. In contrast, in the generated microstructure, it was discretely distributed based on the input images. This difference is substantiated by Table 3, where the number of martensite grains in the observed microstructure is fewer than in the generated microstructure, despite the observed microstructure having a higher volume fraction of the martensite phase. It was difficult to predict the connectivity of the martensite phase from the input images of DP1. Therefore, experimental observations were required to characterize the microscopic morphology. In DP2, while the generated microstructure contains more small grains, it successfully reproduces the overall plate-like structure observed in the 3D microstructure.

2.3. Finite element models

The finite element models of the 3D microstructures were constructed using an image-based modeling

approach to characterize the material behavior based on deformation analysis.

2.3.1. Finite element meshes

The finite element meshes were fabricated using the voxel data of the observed and generated 3D microstructures based on the voxel coarsening approach [30]. The cubic evaluation areas of 171 pixels × 171 pixels × 171 pixels (approximately 5 mega voxels) were extracted from the center of the rectangular space in the four structures depicted in Figures 2 and 4. The size of the extracted area depended on the minimum dimension of the overall structure. Specifically, the side lengths of the extracted area were 67.1 μm in DP1 and 88.2 μm in DP2, respectively. Figures 5 and 6 depict the coarsened meshes, wherein one-eighth of the total area is transparentized to indicate the subunits of finer discretization because the finer discretization area cannot be observed from the surfaces of the finite element models. The coarsening approach reduced the number of elements by over 80% while preserving the mesh resolutions around the phase-boundary, i.e. the number of elements in the finite element model of the generated DP2 was 608,313 (12.2% of the original voxel mesh).

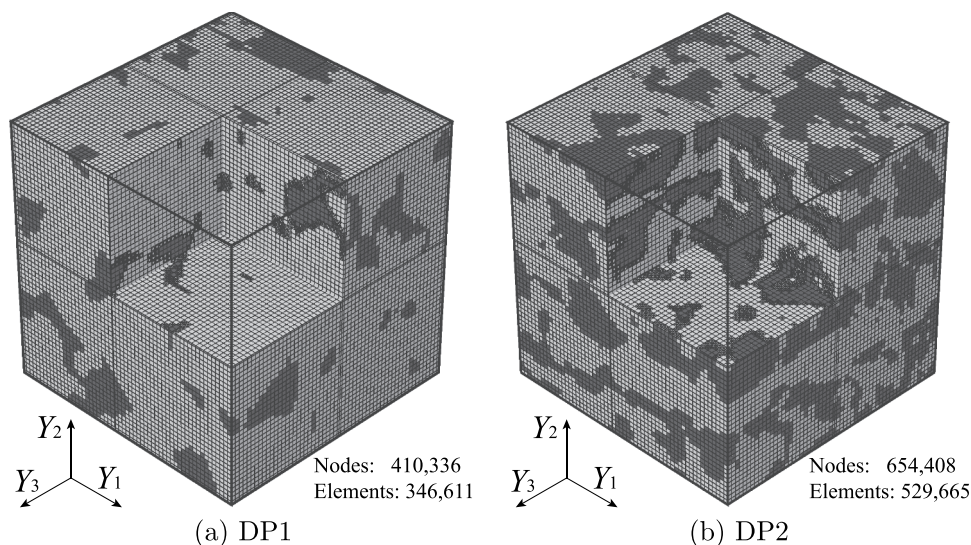


Figure 5. Finite element meshes of the observed 3D microstructures.

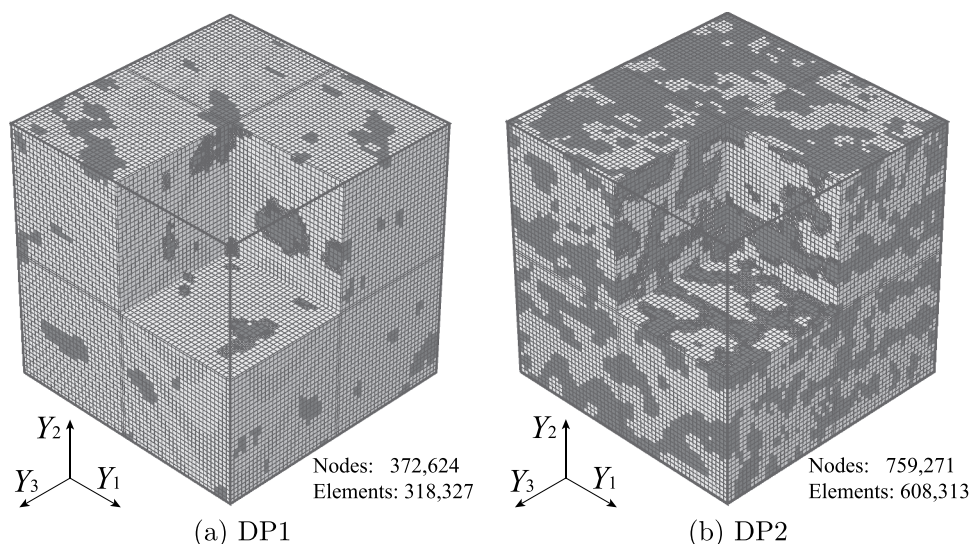


Figure 6. Finite element meshes of the generated 3D microstructures.

Table 4. Volume fraction of the martensite phase in finite element models.

	DP1		DP2	
	observed	generated	observed	generated
Volume fraction [%]	14.5	10.7	41.5	43.8

The finite element meshes are adequately refined to evaluate material properties such as macroscopic yield strength, which typically shows minimal sensitivity to mesh size [31]. It was assumed that the phase-boundary does not slip and debond in this study.

Although these 3D microstructures were non-periodic, finite element analysis method for periodic microstructure was employed owing to its reduction of the adverse boundary effect. The periodic boundary condition can be applied without any modifications because the surface mesh retains its lattice structure in

the coarsening approach. Table 4 lists the volume fractions of martensite phase in the finite element models, which are in agreement with the observed and generated 3D microstructures in Table 3. Furthermore, the morphological feature of the finite element model was similar to the objective 3D microstructure when the extraction area was varied; hence, this area can be considered as a representative volume element. This implies that the size of the extracted area is sufficiently large and suitable for the finite element model to accurately evaluate material properties.

2.3.2. Constitutive models

An isotropic elastoplastic constitutive model was employed to characterize the mechanical properties of the ferrite and martensite phases; i.e. the crystallographic anisotropy was assumed to be minor in comparison with the difference of the yield strengths between the phases. The elastic properties of the two phases were assumed to be the same; the Young's modulus and Poisson's ratio were defined as 210 GPa and 0.3, respectively. For plasticity, we invoked the von Mises stress yield criterion and Swift type hardening law described as $\sigma_Y = a(b + \epsilon^p)^n$. Table 5 lists the plastic material constants based on the experimental database characterized by the alloy compositions and major strengthening factors [32]. Here, the ideal alloy compositions of the ferrite and martensite phases in DP1 and DP2 were assumed based on thermo-dynamic equilibrium [33], as detailed in Table 6. Carbon partitioning was calculated using the Fe – C equilibrium diagram. Therefore, the material constants were determined without relying on experimental mechanical tests. Figure 7 shows the equivalent stress–strain curves of each phase in DP1 and DP2, in which the equivalent stress and strain are defined as follows:

$$\begin{aligned} \sigma^* &:= \sqrt{\frac{3}{2} \text{dev}[\sigma] : \text{dev}[\sigma]} \quad \text{and} \\ \epsilon^* &:= \sqrt{\frac{2}{3} \text{dev}[\epsilon] : \text{dev}[\epsilon]}, \end{aligned} \quad (1)$$

where σ and ϵ are the Cauchy stress and the logarithmic strain tensors at current configuration, respectively. The material responses of the ferrite phase were nearly identical for both samples. In contrast, the response of martensite phase in DP2 was stronger than that in DP1 owing to the difference in carbon content.

3. Deformation analyses of 3D microstructures

We performed the deformation analyses of the 3D microstructures prepared in Section 2 to characterize their macroscopic material properties. The variations between the observed and generated microstructures are discussed.

3.1. Finite element analysis method for periodic microstructure

The boundary value problem for a periodic microstructure is defined at micro-scale \mathbf{Y} as follows:

$$\int_{\Omega_Y} \mathbf{P} : \nabla_Y \eta d\Omega_Y = 0 \quad \forall \eta \in W_{\text{periodic}}, \quad (2)$$

where $\tilde{\mathbf{u}}$ and η denote the microscopic periodic displacement and its variation, respectively; \mathbf{P} is the first Piola–Kirchhoff stress; Ω_Y is the volume of the periodic microstructure; and W_{periodic} represents the Sobolev

Table 5. Plastic material constants of the ferrite and martensite phases in DP1 and DP2.

Phase		a [GPa]	b	n
Ferrite	DP1	0.5851	0.0020	0.1263
	DP2	0.5857	0.0020	0.1279
Martensite	DP1	1.774	10^{-7}	0.04530
	DP2	1.841	10^{-7}	0.04669

Table 6. Estimated chemical compositions of ferrite and martensite phases in dual-phase steel samples for determination of plastic material constants.

[wt%]		C	Si	Mn	P
DP1	Ferrite	0.0012	0.49	–	0.001
	Martensite	0.21	–	2.01	–
DP2	Ferrite	0.0013	0.50	–	0.001
	Martensite	0.23	–	1.99	–

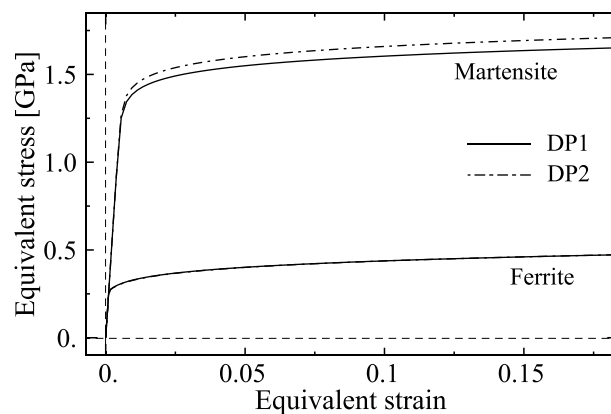


Figure 7. Equivalent stress–strain curves of the ferrite and martensite phases.

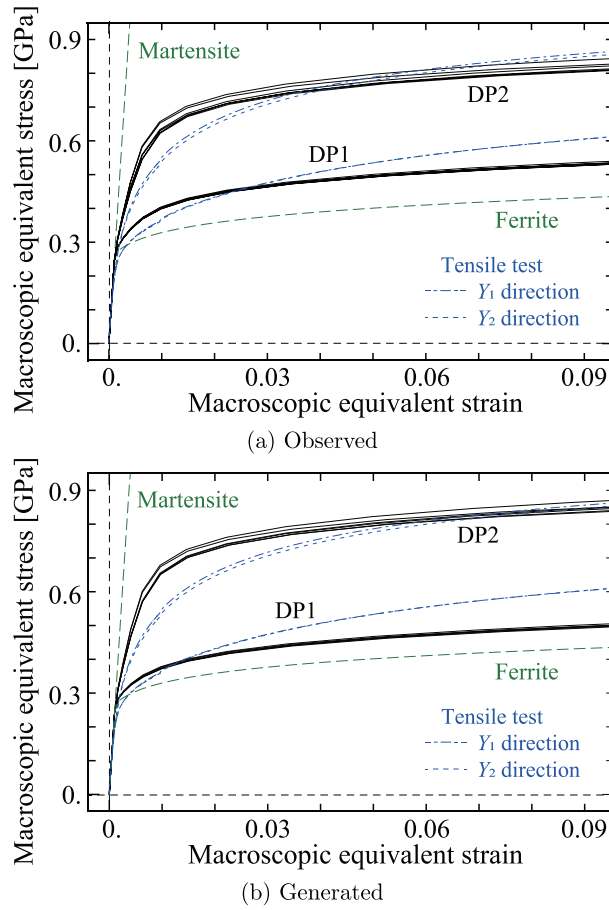


Figure 8. Macroscopic equivalent stress – strain curves.

space of periodic functions. Based on two-scale kinematics [34], the displacement field at micro-scale Y can be divided into macroscopic homogeneous displacement and microscopic periodic displacement as follows:

$$u = \bar{H}Y + \tilde{u} \quad (3)$$

where \bar{H} is the macroscopic displacement gradient. Accordingly, the microscopic displacement gradient H can be formulated as follows:

$$H = \nabla_Y u = \bar{H} + \nabla_Y \tilde{u}. \quad (4)$$

A macroscopic variable $\bar{\bullet}$ is defined by the volume average of the corresponding microscopic variable \bullet as follows:

$$\bar{\bullet} = \frac{1}{\Omega_Y} \int_{\Omega_Y} \bullet d\Omega_Y. \quad (5)$$

Finite element analysis was performed by controlling macroscopic displacement gradient \bar{H} as a boundary condition [11]. The anisotropic material behaviors

were characterized by imposing the macroscopic displacement gradient tensors corresponding to the tensile and compression tests on 3D microstructures as

$$\bar{H} = \begin{bmatrix} \varepsilon_{\text{axial}} & 0 & 0 \\ 0 & * & 0 \\ 0 & 0 & * \end{bmatrix} \quad (6)$$

which is the case for the tensile deformation along the Y_1 direction. In Equation (6), $\varepsilon_{\text{axial}}$ is the imposed axial strain value and $*$ is the unknown value calculated via finite element analysis. Notably, the finite element analysis for periodic microstructures is independent of the length scale of RVE because of the underlying mathematical formulation [34].

3.2. Results and discussion

3.2.1. Macroscopic aspect

Figure 8 shows the resulting macroscopic equivalent stress – strain curves with the results of the

Table 7. Loading stress state.

[GPa]		$\varepsilon^* = 0.01$			$\varepsilon^* = 0.05$		
model		Average	Min	Max	Average	min	max
DP1	Observed	0.40137	0.39918	0.40489	0.49586	0.49303	0.50074
	Generated	0.37529	0.37215	0.37921	0.46271	0.45896	0.46761
DP2	Observed	0.63980	0.62538	0.66013	0.77727	0.76508	0.79727
	Generated	0.66401	0.65413	0.68201	0.80454	0.79480	0.82261

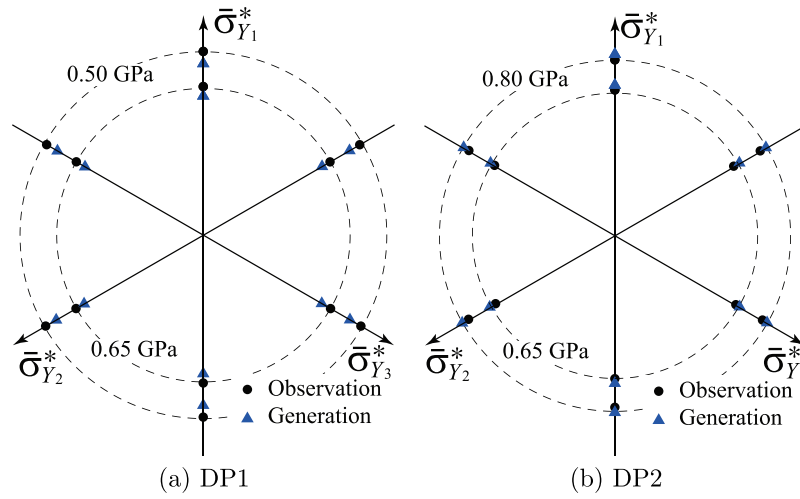


Figure 9. Equivalent stress states on the deviatoric stress plane at equivalent strains of 0.01 and 0.05.

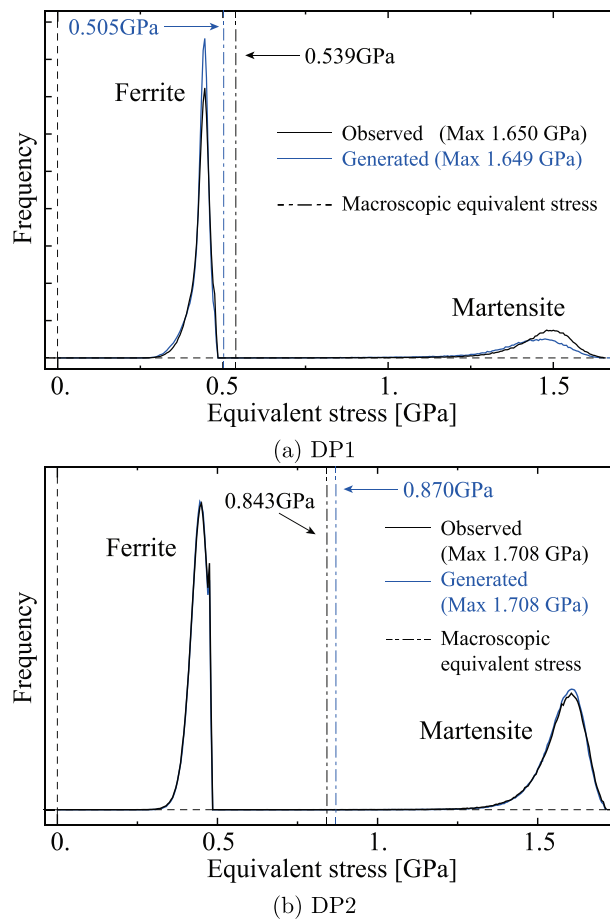


Figure 10. Histograms of equivalent stress at a macroscopic axial strain of 0.10 in the uniaxial tensile stress along the Y_1 direction.

experimental tensile tests on DP1 and DP2 along the Y_1 and Y_2 directions. The macroscopic equivalent stress and strain were calculated from the macroscopic stress and strain tensors. The strain was defined as the logarithmic strain at current configuration, $\varepsilon = \frac{1}{2} \ln \left[(1 + \bar{\mathbf{H}})(1 + \bar{\mathbf{H}})^T \right]$, where $\mathbf{1}$ is the second-order identity tensor. The differences between the experimental and computational results for both samples

have also been shown. In particular, the computational results indicate a high yield strength and low hardening ratio in all cases compared to the experimental results. These were caused by variations in the plastic properties of each phase and volume fraction of the martensite/ferrite phase. However, the material responses, such as the stress level and anisotropic response, were relatively characterized without fitting to the experimental tensile tests.

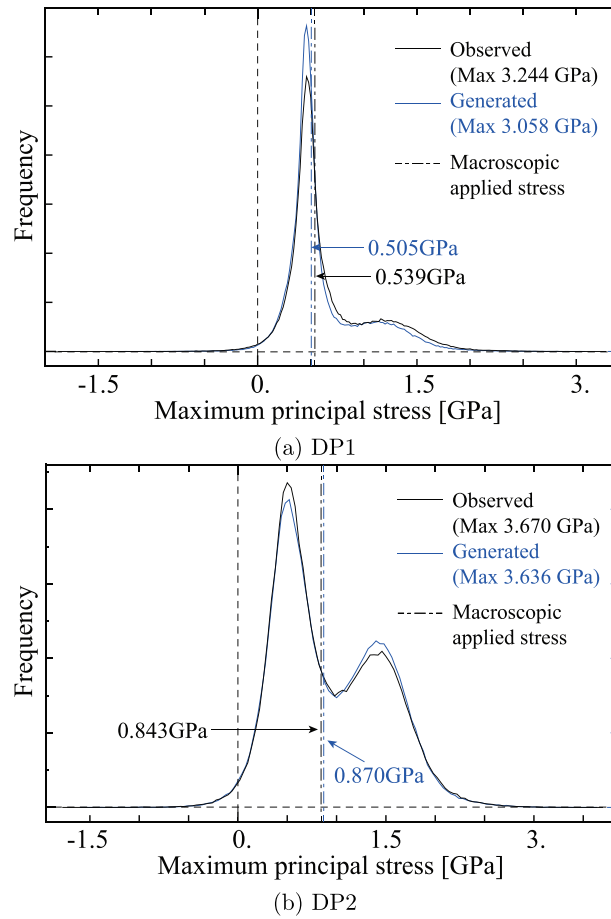
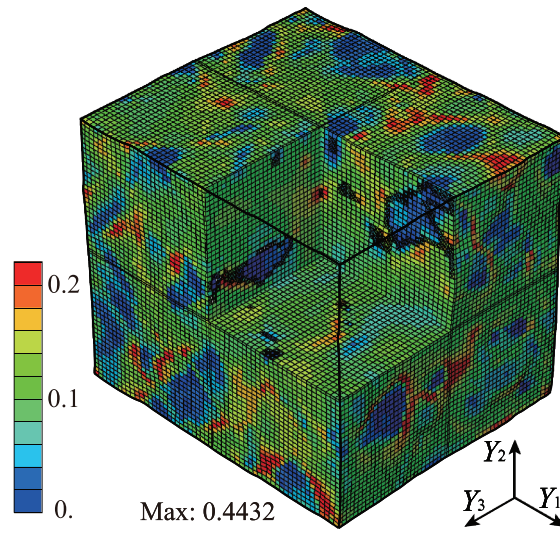


Figure 11. Histograms of maximum principal stress at a macroscopic axial strain of 0.10 in the uniaxial tensile stress along the Y_1 direction.

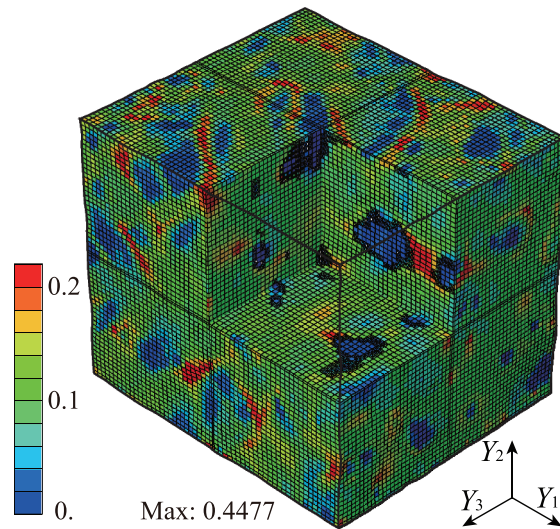
The loading stress states of each case are plotted on the deviatoric stress plane, i.e. the π -plane, in Figure 9 and summarized in Table 7. The stresses of the generated cases were approximately 6.5% lower and 3.5% higher than those in the observed cases of DP1 and DP2, respectively. This result corresponds to the relationship between the volume fractions of the martensite phase. In DP1, the material responses of the observed and generated microstructures were nearly isotropic. Despite different microscopic morphologies, the difference between the maximum and minimum stresses was less than 0.01 GPa at $\epsilon^* = 0.05$ and the morphological effects were insignificant. Contrastingly, the anisotropic material responses were observed in DP2, wherein the difference between the maximum and minimum stresses was over 0.27 GPa at $\epsilon^* = 0.05$. The loading stresses for tensile deformation along the Y_1 direction were the highest for the observed and generated microstructures. The anisotropic material responses were caused by the microscopic morphology. Therefore, the morphological features of the microstructure were reproduced in the generation of DP2. The evaluated anisotropic properties in DP1 and DP2 were agreed with the experimental results as shown in Figure 9.

3.2.2. Microscopic aspect

Figures 10 and 11 present the histograms of the equivalent and maximum principal stresses in the finite element models when tension is applied along the Y_1 direction. The stresses are calculated at the center of each element. The distributions of equivalent stresses are distinctly separated into ferrite and martensite phases in both figures. In DP1, the equivalent stress distribution in the martensite phase differs between the observed and generated microstructures, with the generated microstructure exhibiting higher stress. This difference in stress distribution is because of variations in the geometry of the microstructure. Specifically, the martensite phase, having higher strength, experiences higher stress to achieve the same axial strain when it is continuously distributed throughout the microstructure. Consequently, the maximum value of the maximum principal stress is higher in the observed microstructure compared to the generated one. It is important to note that the maximum principal stress is associated with damage initiation. In DP2, the stress distributions and their maximum values are similar between the observed and generated microstructures. Therefore, the generated



(a) Observed



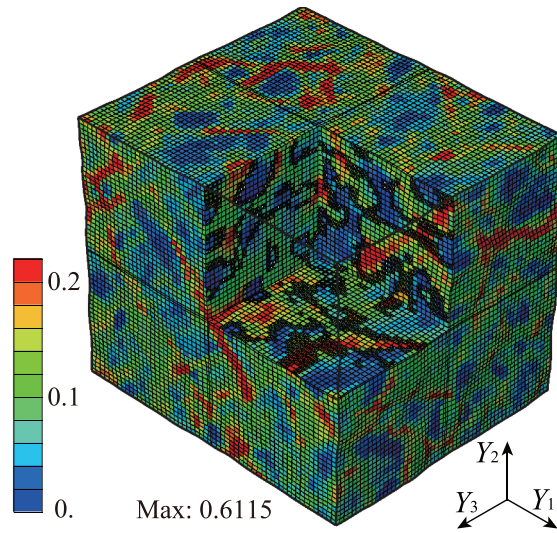
(b) Generated

Figure 12. Equivalent plastic strain distribution in the DP1 microstructure at a macroscopic axial strain of 0.10 in the uniaxial tensile stress along the Y_1 direction.

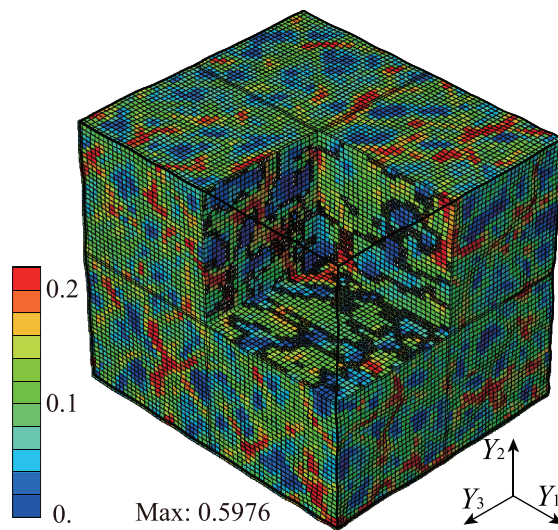
microstructure accurately replicates the deformation state of the observed microstructure.

Figures 12 and 13 show the distributions of the accumulated equivalent plastic strain in the deformed microstructures when the tension is along the Y_1 direction, in which one-eighth of the total area is transparent. Additionally, Figure 14 shows histograms

of the accumulated equivalent plastic strain in the finite element models when tension is applied along the Y_1 direction, with stresses calculated at the center of each element. The plastic deformation is heterogeneously distributed. It has been confirmed that finite element analysis of a duplex steel microstructure can reproduce the deformation state by comparison with



(a) Observed



(b) Generated

Figure 13. Equivalent plastic strain distribution in the DP2 microstructure at a macroscopic axial strain of 0.10 in the uniaxial tensile stress along the Y_1 direction.

the experimental result measured by digital image correlation method [35]. In DP1, the distribution of equivalent plastic strain is divided into ferrite and martensite phases, similar to the stress distribution, revealing differences in the deformation state. In contrast, the distributions in DP2 are continuous and similar between the observed and generated microstructures. These results suggest that differences in

microstructure geometry lead to incorrect evaluations, particularly in microscopic deformation analysis, rather than differences in volume fraction. This geometrical effect is significant, especially in cases with a low volume fraction of the martensite phase. Therefore, reproducibility must be improved for practical applications as plastic strain localization and damage initiation within the microstructure

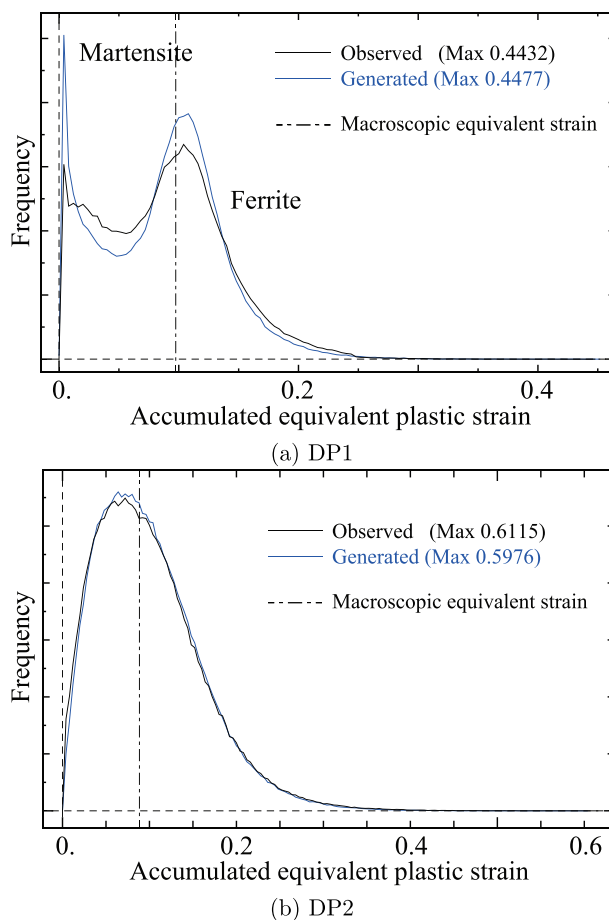


Figure 14. Histograms of equivalent plastic strain at a macroscopic axial strain of 0.10 in the uniaxial tensile stress along the Y_1 direction.

significantly affect the material performance in dual-phase steels [24,25,27]. An obvious solution is to incorporate some serial sectioning images, even if only a few, into the input data. Utilizing deep-learning-based technology remains beneficial in this approach.

4. Conclusions

Using finite element analyses of representative volume elements, this study compared the 3D microstructures of ferrite – martensite dual-phase steels generated by SliceGAN with the experimentally observed microstructures in the macroscopic material responses. The generation algorithm characterized the microscopic morphology of the surface images; however, it could not accurately reproduce the volume fractions of the martensite/ferrite phases. Consequently, the macroscopic loading stresses exhibited variations between the observed and generated 3D microstructures. The reproducibility can be improved by applying constraints to the volume fraction. Besides, the algorithm could not reproduce the microscopic morphology in DP1. In this case, it was difficult to predict the morphology from the input images. Therefore, although the deep-learning-based generation

algorithm can provide 3D microstructures with less effort, experimental 3D observations are required to characterize the microscopic morphology.

Highlights

- Microstructures of two dual-phase steels were generated with SliceGAN.
- Mechanical responses of 3D microstructures were compared with experimentally observed microstructures.
- Image-based finite element analyses were performed for generated and observed microstructures.
- Macroscopic anisotropic responses of the microstructures were evaluated.
- The generated microstructures were validated from views of macro- and microscopic material behaviors.

Acknowledgments

The authors wish to acknowledge Ms. Y. Yamamoto and Dr. S. Taniguchi of the National Institute for Materials Science for their technical support. We would like to thank Editage for English language editing

Disclosure statement

No potential conflict of interest was reported by the author(s).

Funding

This research was financially supported by JSPS KAKENHI [grant number 21H01220, 22H01807].

ORCID

Ikumu Watanabe  <http://orcid.org/0000-0002-7693-1675>

Ta-Te Chen  <http://orcid.org/0000-0002-0553-4736>

Toshio Ogawa  <http://orcid.org/0000-0001-8541-9932>

Yoshitaka Adachi  <http://orcid.org/0000-0002-2190-1399>

Code availability

The code used in this study to generate 3D microstructure is available at <https://github.com/KeiyaSugiura/3d-microstructure-generation>

References

- [1] Kolken HM, Zadpoor A. Auxetic mechanical metamaterials. *RSC Adv.* 2017;7(9):5111–5129. doi: 10.1039/C6RA27333E
- [2] Zheng X, Guo X, Watanabe I. A mathematically defined 3d auxetic metamaterial with tunable mechanical and conduction properties. *Mater & Des.* 2021;198:109313. doi: 10.1016/j.matdes.2020.109313
- [3] Zheng X, Watanabe I, Wang S, et al. Minimal-surface-based multiphase metamaterials with highly variable stiffness. *Mater & Des.* 2024;237:112548. doi: 10.1016/j.matdes.2023.112548
- [4] Zhou J, Watanabe I, Song W, et al. Multi-objective topology optimization of porous microstructure in die-bonding layer of a semiconductor. *Sci Technol Adv Mater: Methods.* 2024;4(1):2320691. doi: 10.1080/27660400.2024.2320691
- [5] Lee D, Chen W, Wang L, et al. Data-driven design for metamaterials and multiscale systems: a review. *Adv Mater.* 2024;36(8):2305254. doi: 10.1002/adma.202305254
- [6] Zheng X, Chen TT, Jiang X, et al. Deep-learning-based inverse design of three-dimensional architected cellular materials with the target porosity and stiffness using voxelized voronoi lattices. *Sci Technol Adv Mater.* 2023;24(1):2157682. doi: 10.1080/14686996.2022.2157682
- [7] Olson GB. Computational design of hierarchically structured materials. *Science.* 1997;277(5330):1237–1242. doi: 10.1126/science.277.5330.1237
- [8] Xiong W, Olson GB. Cybermaterials: materials by design and accelerated insertion of materials. *NPJ Comput Mater.* 2016;2(1):1–14. doi: 10.1038/npjcompumats.2015.9
- [9] Kimura Y, Inoue T, Yin F, et al. Inverse temperature dependence of toughness in an ultrafine grain-structure steel. *Science.* 2008;320(5879):1057–1060. doi: 10.1126/science.1156084
- [10] Koseki T, Inoue J, Nambu S. Development of multi-layer steels for improved combinations of high strength and high ductility. *Mater Trans.* 2014;55(2):227–237. doi: 10.2320/matertrans.M2013382
- [11] Watanabe I, Nakamura G, Yuge K, et al. Maximization of strengthening effect of microscopic morphology in duplex steels. Cham: Springer International Publishing; 2015. Chapter 24; p. 541–555. doi: 10.1007/978-3-319-19440-0_24
- [12] Orlov D, Ameyama K. Critical assesment 37: harmonic-structure materials-idea, status and perspectives. *Mater Sci Technol.* 2020;36(5):517–526. doi: 10.1080/02670836.2020.1719306
- [13] Hayashi Y, Setoyama D, Hirose Y, et al. Intragranular three-dimensional stress tensor fields in plastically deformed polycrystals. *Sci.* 2019;366(6472):1492–1496. doi: 10.1126/science.aax9167
- [14] Wang Y, Toda H, Xu Y, et al. In-situ 3d observation of hydrogen-assisted particle damage behavior in 7075 al alloy by synchrotron x-ray tomography. *Acta Materialia.* 2022;227:117658. doi: 10.1016/j.actamat.2022.117658
- [15] Sato N, Adachi Y, Kawata H, et al. Topological approach to ferrite/martensite dual-phase microstructures. *ISIJ Int.* 2012;52(7):1362–1365. doi: 10.2355/isijinternational.52.1362
- [16] Nishikawa H, Furuya Y, Osada T, et al. Three-dimensional high-resolution crystallographic observation of the entire volume of microstructurally small fatigue cracks in ni-co based superalloy. *Scr Materialia.* 2023;222:115026. doi: 10.1016/j.scriptamat.2022.115026
- [17] Turner DM, Kalidindi SR. Statistical construction of 3-d microstructures from 2-d exemplars collected on oblique sections. *Acta Materialia.* 2016;102:136–148. doi: 10.1016/j.actamat.2015.09.011
- [18] Fu J, Xiao D, Li D, et al. Stochastic reconstruction of 3d microstructures from 2d cross-sectional images using machine learning-based characterization. *Comput Methods In Appl Mech And Eng.* 2022;390:114532. doi: 10.1016/j.cma.2021.114532
- [19] Bostanabad R. Reconstruction of 3d microstructures from 2d images via transfer learning. *Comput-Aided Des.* 2020;128:102906. doi: 10.1016/j.cad.2020.102906
- [20] Zhang F, Teng Q, Chen H, et al. Slice-to-voxel stochastic reconstructions on porous media with hybrid deep generative model. *Comput Mater Sci.* 2021;186:110018. doi: 10.1016/j.commatsci.2020.110018
- [21] Kench S, Cooper SJ. Generating three-dimensional structures from a two-dimensional slice with generative adversarial network-based dimensionality expansion. *Nat Mach Intell.* 2021;3(4):299–305. doi: 10.1038/s42256-021-00322-1
- [22] Sugiura K, Ogawa T, Adachi Y. Hourly work of 3d microstructural visualization of dual phase steels by sliceGAN. *Advcd Theory Sims.* 2022;5(7):2200132. doi: 10.1002/adts.202200132
- [23] Sugiura K, Ogawa T, Adachi Y, et al. Big-volume sliceGAN for improving a synthetic 3d microstructure image of additive-manufactured type 316l steel. *J Imag.* 2023;9(5):90. doi: 10.3390/jimaging9050090
- [24] Sun X, Choi KS, Liu WN, et al. Predicting failure modes and ductility of dual phase steels using plastic strain localization. *Int J Plasticity.* 2009;25(10):1888–1909. doi: 10.1016/j.ijplas.2008.12.012
- [25] Lian J, Yang H, Vajragupta N, et al. A method to quantitatively upscale the damage initiation of dual-phase steels under various stress states from

- microscale to macroscale. *Comput Mater Sci.* 2014;94:245–257. doi: [10.1016/j.commatsci.2014.05.051](https://doi.org/10.1016/j.commatsci.2014.05.051)
- [26] Zhou J, Gokhale AM, Gurumurthy A, et al. Realistic microstructural rve-based simulations of stress–strain behavior of a dual-phase steel having high martensite volume fraction. *Mater Sci Eng: A.* 2015;630:107–115. doi: [10.1016/j.msea.2015.02.017](https://doi.org/10.1016/j.msea.2015.02.017)
- [27] Alaie A, Rad SZ, Kadkhodapour J, et al. Effect of microstructure pattern on the strain localization in dp600 steels analyzed using combined in-situ experimental test and numerical simulation. *Mater Sci Eng: A.* 2015;638:251–261. doi: [10.1016/j.msea.2015.04.071](https://doi.org/10.1016/j.msea.2015.04.071)
- [28] Abid NH, Al-Rub RKA, Palazotto AN. Micromechanical finite element analysis of the effects of martensite morphology on the overall mechanical behavior of dual phase steel. *Int J Solids And Struct.* 2017;104:8–24. doi: [10.1016/j.ijsolstr.2016.11.005](https://doi.org/10.1016/j.ijsolstr.2016.11.005)
- [29] Matsuno T, Yoshioka T, Watanabe I, et al. Three-dimensional finite element analysis of representative volume elements for characterizing the effects of martensite elongation and banding on tensile strength of ferrite-martensite dual-phase steels. *Int J Mech Sci.* 2019;163:105133. doi: [10.1016/j.ijmecsci.2019.105133](https://doi.org/10.1016/j.ijmecsci.2019.105133)
- [30] Watanabe I, Yamanaka A. Voxel coarsening approach on image-based finite element modeling of representative volume element. *Int J Mech Sci.* 2019;150:314–321. doi: [10.1016/j.ijmecsci.2018.10.028](https://doi.org/10.1016/j.ijmecsci.2018.10.028)
- [31] Watanabe I, Terada K, de Souza Neto EA, et al. Characterization of macroscopic tensile strength of polycrystalline metals with two-scale finite element analysis. *J Mech And Phys Solids.* 2008;56(3):1105–1125. doi: [10.1016/j.jmps.2007.06.001](https://doi.org/10.1016/j.jmps.2007.06.001)
- [32] Tsuchida N, Harjo S, Ohnuki T, et al. Stress-strain curves of steels. *Tetsu-To-Hagane.* 2014;100(10):1191–1206. doi: [10.2355/tetsutohagane.100.1191](https://doi.org/10.2355/tetsutohagane.100.1191)
- [33] Fukatsu Y, Chen TT, Ogawa T, et al. Analysis of the strength–ductility balance of dual-phase steel using a combination of generative adversarial networks and finite element method. *Comput Mater Sci.* 2024;243:113143. doi: [10.1016/j.commatsci.2024.113143](https://doi.org/10.1016/j.commatsci.2024.113143)
- [34] Terada K, Saiki I, Matsui K, et al. Two-scale kinematics and linearization for simultaneous two-scale analysis of periodic heterogeneous solids at finite strain. *Comput Methods In Appl Mech And Eng.* 2003;192(31–32):3531–3563. doi: [10.1016/S0045-7825\(03\)00365-7](https://doi.org/10.1016/S0045-7825(03)00365-7)
- [35] Watanabe I, Setoyama D, Nagasako N, et al. Multiscale prediction of mechanical behavior of ferrite–pearlite steel with numerical material testing. *Int J For Numer Methods In Eng.* 2012;89(7):829–845. doi: [10.1002/nme.3264](https://doi.org/10.1002/nme.3264)